crystals

MDPI

Article

It Is Getting Packed in Here: Synthesis, Structure and Biological Activity of Halogenated 1,10-Phenanthroline Epoxide Derivatives

Julian Polle [1], Florian Mai [1], Marcus Layh [1], Verena Spiegler [2] and Marian Hebenbrock [1,*]

[1] Institute of Inorganic and Analytical Chemistry, University of Münster, Corrensstr. 28/30, 48149 Münster, Germany
[2] Institute for Pharmaceutical Biology and Phytochemistry, University of Münster, Corrensstraße 48, 48149 Münster, Germany
* Correspondence: hebenbro@uni-muenster.de

Abstract

1,10-Phenanthroline derivatives are versatile ligands whose structural and biological properties can be tuned by targeted functionalization. Here, a series of 2,9-dihalogenated 1,10-phenanthroline derivatives and their corresponding 5,6-epoxy-5,6-dihydro analogs were synthesized and characterized. Single-crystal X-ray diffraction experiments reveal pronounced substituent-dependent packing motifs. While 2,9-diiodo-1,10-phenanthroline forms a sandwich-herringbone arrangement dominated by short I···I contacts, the phenanthroline epoxides exhibit π-stacking combined with C–H···O and C–H···halogen interactions. For the brominated and iodinated epoxides, additional halogen···halogen contacts generate extended supramolecular networks. Biological evaluation in selected cell lines showed that both halogenation and epoxidation reduce the cytotoxicity of the parent phenanthroline scaffold, whereas no significant effects on *Pseudomonas aeruginosa* growth or biofilm formation were observed. These results demonstrate how simple structural modifications of 1,10-phenanthroline influence both solid-state organization and biological activity, providing insight into the role of halogen substituents and epoxide formation in phenanthroline-based systems.

Keywords: 1,10-phenanthroline; phenanthroline epoxides; halogen···halogen interactions; supramolecular chemistry; cytotoxicity

1. Introduction

1,10-Phenanthroline and its derivatives are well-established chelating ligands for the preparation of functional transition-metal complexes [1,2]. Their coordination chemistry enables the combination of the intrinsic ligand properties, which arise from the extended π-system and planar aromatic structure, with the characteristic electronic, redox, magnetic, and photophysical properties of metal ions. Owing to the pronounced chelate effect associated with the N,N′-diimine binding motif, such complexes often exhibit high thermodynamic and kinetic stability, rendering them suitable for a broad range of applications [1,2].

One major area of application is catalysis, particularly photocatalysis, because the electronic and steric properties of phenanthroline-based complexes can be readily tuned through relatively small modifications of the ligand framework [1,3]. Beyond catalysis, these complexes have also attracted considerable attention for potential therapeutic applications, mainly due to their diverse biological activities.

Academic Editor: Jane S. Murray

Received: 13 July 2026
Revised: 25 August 2026
Accepted: 26 August 2026
Published: 7 September 2026

For example, copper complexes of 1,10-phenanthroline derivatives can exhibit artificial nuclease-like activity toward DNA [4]. Palladium(II) complexes containing phenanthroline ligands have also been reported to display pronounced cytotoxicity, including activity against cisplatin-resistant cell lines, which has been attributed in part to their interaction with nucleic acids [5]. Furthermore, phenanthroline-based metal complexes may increase intracellular oxidative stress and thereby exert antibacterial effects, as demonstrated, for instance, for chromium complexes [6].

Several other phenanthroline metal complexes have likewise shown cytotoxic properties in different cellular models, including silver, gold, platinum, palladium, copper, and vanadium systems [6–12]. In some cases, this cytotoxicity has been associated with the formation of reactive oxygen species and therefore the induction of oxidative stress [11].

However, studies on phenanthroline-based vanadium(IV) complexes have shown that the biological activity of such compounds does not necessarily originate from the intact metal complex. Instead, decomposition of the complex under biological conditions can release the phenanthroline ligand, which may subsequently form new complexes with redox-active endogenous metal ions such as Cu(II) and Fe(II). These in situ formed species can then contribute to cytotoxicity, for example through oxidative-stress-related mechanisms [12]. This observation highlights the importance of distinguishing between the biological effects of the intact metal complex and those arising from ligand release or secondary complex formation in the biological medium.

This is also reflected in studies investigating the biological activity of uncoordinated 1,10-phenanthroline derivatives. Uncoordinated 1,10-phenanthroline itself displays micromolar activity in selected cell lines, although without pronounced selectivity toward cancer cells [13]. Interestingly, the oxidized derivative 1,10-phenanthroline-5,6-dione shows increased activity compared with the parent compound. However, this enhanced potency is not necessarily accompanied by improved selectivity, since activity has also been observed against non-tumorigenic HK-2 normal renal cells and Chang normal liver cells [13].

In addition to cytotoxic effects in mammalian cells, 1,10-phenanthroline and its derivatives also exhibit antifungal activity [9,14]. The increased activity of 1,10-phenanthroline-5,6-dione (phendione) against Candida albicans has been attributed to the combination of the chelating N,N′-diimine motif with a redox-active quinonoid unit [14]. Thus, the biological activity of phenanthroline derivatives appears to arise from a combination of metal-chelating ability, redox activity, planar aromatic structure, and potential interactions with biomolecular targets such as nucleic acids.

The present study aims to address this point by investigating the so far scarcely explored epoxide derivatives of 1,10-phenanthroline with respect to both their molecular structure and biological activity. In particular, the coordinating properties of the N,N′-diimine unit will be modulated through halogenation, which is expected to influence both the structural characteristics and the biological behavior of the compounds. For comparison, the corresponding non-epoxidized derivatives will also be examined.

2. Materials and Methods

2.1. General Aspects

All chemicals used in this study were of p.a. grade and were obtained from ABCR (Karlsruhe, Germany), Acros Organics (Geel, Belgium), Alfa Aesar (Ward Hill, MA, USA), AppliChem (Darmstadt, Germany), BLDpharm (Shanghai, China), Carl Roth (Karlsruhe, Germany), Fisher Scientific (Pittsburgh, PA, USA), Fluorochem (Glossop, UK), Merck (Darmstadt, Germany), Sigma-Aldrich (Burlington, MA, USA), TCI (Tokyo, Japan) or VWR (Radnor, PA, USA) and used, if not stated otherwise, without further purification.

NMR spectra were recorded on AVANCE NEO 400 (Bruker, Billerica, MA, USA) and AVANCE NEO 500 (Bruker) NMR spectrometers. Chemical shifts are reported as δ, parts per million (ppm), and referenced to internal solvent residues. Coupling constants J are stated in Hertz (Hz). The following abbreviations are used for spin multiplicities: s (singlet), d (doublet), t (triplet), q (quartet), dd (doublet of doublet), m (multiplet). High-resolution ESI-MS spectra were recorded on an Impact II VIP QTOF ESI-MS (Bruker).

Elemental analysis was performed on a vario EL III CHNS (Elementar Analysensysteme GmbH, Langenselbold, Germany).

*2.2. 2,9-Difluoro-[1,10]phenanthroline (**2**) [15]*

Prior to the reaction, all glassware was dried, and 18-crown-6 was recrystallized and stored under argon. Tetramethylammonium chloride (0.132 g, 1.20 mmol, 0.15 eq.) and 18-crown-6 (0.317 g, 1.20 mmol, 0.15 eq.) were dissolved in dry DMSO (20 mL, dried over molecular sieves) together with 2,9-dichloro-[1,10]phenanthroline (**3**) (2.00 g, 8.03 mmol, 1.00 eq.). The mixture was heated to 100 °C and stirred for 30 min. Afterward, CsF (7.32 g, 48.2 mmol, 6.00 eq.) was added, and the mixture was then stirred at 100 °C for another 4 h. The hot mixture was poured onto ice, and the raw product was extracted with DCM (3 × 50 mL). The combined organic phases were dried over $MgSO_4$, and the solvent was removed under reduced pressure. Residues of DMSO were removed under high vacuum. The white product was purified through column chromatography (silica gel, DCM/TEA 100:1, R_f = 0.3). The product was obtained as a white powder (1.61 g, 7.44 mmol, 93%). ^{1}H NMR: (500 MHz, DMSO-d_6, ppm) δ = 8.74 (dd, $^3J_{HH}$ = 8.7 Hz, $^4J_{HF}$ = 8.2 Hz, 2H, H4, H7), 8.08 (s, 2H, H5, H6), 7.61 (dd, $^3J_{HH}$ = 8.7 Hz, $^3J_{HF}$ = 3.1 Hz, 2H, H3, H8). ^{13}C{^{1}H} NMR: (126 MHz, DMSO-d_6, ppm) δ = 161.1 (d, $^1J_{CF}$ = 239 Hz, C2, C9), 143.1 (d, $^3J_{CF}$ = 9.4 Hz, C4, C7), 142.0 (d, $^3J_{CF}$ = 15.8 Hz, C10a, C10b), 127.7 (d, $^4J_{CF}$ = 2.1 Hz, C4a, C6a), 125.4 (d, $^5J_{CF}$ = 1.9 Hz, C5, C6), 111.7 (d, $^2J_{CF}$ = 41.8 Hz, C3, C8). ^{15}N{^{1}H} NMR: (51 MHz, DMSO-d_6, ppm) δ = 259 (N1, N10). ^{19}F{^{1}H} NMR (471 MHz, DMSO-d_6, ppm): δ = −61.9 (F2, F9). ESI(+)-HRMS: (m/z) calcd. for $[C_{12}H_6N_2F_2+H]^+$ = 217.0576; found: 217.0577.

*2.3. 2,9-Diiodo-[1,10]phenanthroline (**5**) [16,17]*

2,9-Dichloro-[1,10]phenanthroline (**3**) (2.01 g, 8.03 mmol, 1.00 eq.) was suspended in HI (65%, 18 mL). The suspension was heated to 105 °C and stirred at this temperature for 3 days. Afterward, the reaction mixture was cooled to room temperature and the gray precipitate was filtered. In a small beaker, the precipitate was treated with an aqueous NH_3 solution (25%, 10 mL), turning the gray solid black. The solid was collected by filtration and washed with water (2 × 15 mL). The solid was recrystallized from EtOH, yielding the product as white, needle-like crystals (2.509 g, 5.807 mmol, 72%). ^{1}H NMR: (400 MHz, DMSO-d_6, ppm) δ = 8.20 (d, $^3J_{HH}$ = 8.4 Hz, 2H, H4, H7), 8.16 (d, $^3J_{HH}$ = 8.4 Hz, 2H, H3, H8), 8.03 (s, 2H, H5, H6). ^{13}C{^{1}H} NMR: (101 MHz, DMSO-d_6, ppm) δ = 145.3 (C10a, C10b), 138.0 (C4, C7), 134.5 (C3, C8), 127.9 (C4a, C6a), 127.0 (C5, C6), 120.1 (C2, C9). ^{15}N{^{1}H} NMR: (51 MHz, DMSO-d_6, ppm) δ = 323 (N1, N10). ESI(+)-HRMS: (m/z) calcd. for $[C_{12}H_6N_2I_2+Na]^+$ = 454.8518, found: 454.8517. Elemental analysis: calcd. for $C_{12}H_6N_2I_2$: C 33.4; H 1.4; N 6.5 found: C 33.2; H 1.5; N 6.3. The analytical data are consistent with the literature [16,17].

*2.4. 5,6-Epoxy-5,6-dihydro-[1,10]phenanthroline (**6**) [18]*

In a 1 L round-bottomed flask, [1,10]phenanthroline (2.00 g, 11.1 mmol, 1.00 eq.) was suspended in $CHCl_3$ (60 mL), tetrabutylammonium hydrogensulfate (0.250 g, 0.736 mmol, 0.07 eq.) was added to the mixture, and the suspension was stirred until both compounds were completely dissolved. In a separate beaker, commercial bleach (Dan Klorix, 200 mL, stabilized with a carbonate buffer, 2–5% active chlorine) was carefully adjusted to a pH

value of 8.6 using concentrated sulfuric acid. The bleach solution was added to the flask, and the reaction mixture was stirred vigorously for 75 min at room temperature. Since the reaction is highly sensitive to changes in pH, with values below 8.2 leading to increased formation of chlorinated byproducts, the pH was carefully maintained between 8.6 and 8.2 using solid NaOH (one pellet every 15 min). The reaction was monitored using NMR spectroscopy after extraction of an aliquot of the reaction mixture with $CDCl_3$, determining the optimal reaction time to be 75 min. Then, a solution of Na_2CO_3 (sat., 100 mL) was added, and the reaction mixture was extracted with dichloromethane (5 × 50 mL). The organic phases were combined and washed with water (100 mL) and a solution of Na_2CO_3 (sat., 3·50 mL), and then dried over $MgSO_4$. The solvent was removed under reduced pressure. The off-white solid was purified via column chromatography (EtOAc → EtOAc:acetone 4:1 → EtOAc:acetone 2:1). The product was obtained as a white solid (2.024 g, 10.41 mmol, 94%). ^{1}H NMR: (400 MHz, DMSO-d_6, ppm) δ = 8.81 (dd, $^3J_{HH}$ = 4.7 Hz, $^4J_{HH}$ = 1.8 Hz, 2H, H2, H9), 8.26 (dd, $^3J_{HH}$ = 7.7 Hz, $^4J_{HH}$ = 1.8 Hz, 2H, H4, H7), 7.53 (dd, $^3J_{HH}$ = 7.7 Hz, $^3J_{HH}$ = 4.7 Hz, 2H, H3, H8), 4.84 (s, 2H, H5, H6). ^{13}C{^{1}H} NMR: (101 MHz, DMSO-d_6, ppm) δ = 150.1 (C2, C9), 148.9 (C10a, C10b), 138.6 (C4, C7), 129.7 (C4a, C6a), 123.9 (C3, C8), 54.5 (C5, C6). ^{15}N{^{1}H} NMR: (40 MHz, DMSO-d_6, ppm) δ = 313 (N1, N10). ESI(+)-HRMS (m/z): calcd. for $[C_{12}H_8N_2ONa]^+$ = 219.0534, found: 219.0529. Elemental analysis calcd. for $C_{12}H_8N_2O$: C 73.5; H 4.1; N 14.3, found: C 73.5; H 4.2; N 14.1. The analytical data are consistent with the literature [18].

*2.5. 5,6-Epoxy-5,6-dihydro-2,9-difluoro-[1,10]phenanthroline (**7**)*

The reaction was conducted in a two-neck flask connected to two gas-washing bottles (one empty and one filled with NaOH (6 M) to react with elemental bromine formed during the reaction). Using an ice bath, sulfuric acid (42 mL, 60%) was cooled to 0 °C, and 2,9-difluoro-[1,10]phenanthroline (**2**, 0.216 g, 1.00 mmol, 1.00 eq.) was added. The suspension was stirred until the solid was fully dissolved. $KBrO_3$ (0.183 g, 1.10 mmol, 1.10 eq.) was slowly added over a period of 30 min at 0 °C. The mixture was allowed to slowly warm to room temperature and was stirred for 16 h. The solution was then poured onto ice (100 mL) and diluted with water. In an ice bath, sodium hydroxide was slowly added to the mixture to adjust the pH to approximately 5. The reaction was neutralized by addition of a saturated aqueous solution of $NaHCO_3$. The solution was extracted with DCM (3 × 50 mL), the combined organic layers were dried over $MgSO_4$, and the solvent was removed under reduced pressure. The remaining solid was purified via flash column chromatography (silica gel, DCM:TEA 100:1, R_f = 0.16), and the product was obtained as a white solid (200 mg, 0.86 mmol, 86%). ^{1}H NMR: (500 MHz, DMSO-d_6, ppm) δ = 8.51 (dd, $^3J_{HH}$ = 8.7 Hz, $^4J_{HF}$ = 8.3 Hz, 2H, H4, H7), 7.39 (dd, $^3J_{HH}$ = 8.3 Hz, $^3J_{HF}$ = 3.1 Hz, 2H, H3, H8), 4.92 (s, 2H, H5, H6). ^{13}C [19] NMR: (126 MHz, DMSO-d_6, ppm) δ = 162.7 (d, $^1J_{CF}$ = 238 Hz, C2, C9), 144.8 (d, $^3J_{CF}$ = 8.4 Hz, C4, C7), 146.4 (d, $^3J_{CF}$ = 14.3 Hz, C10a, C10b), 128.6 (d, $^4J_{CF}$ = 3.7 Hz, C4a, C6a), 110.9 (d, $^2J_{CF}$ = 39.1 Hz, C3, C8), 53.7 (d, $^5J_{CF}$ = 0.7 Hz, C5, C6). ^{15}N{^{1}H} NMR: (51 MHz, DMSO-d_6, ppm) δ = 268 (N1, N10). ^{19}F{^{1}H} NMR (471 MHz, DMSO-d_6, ppm): δ = −65.7 (F2, F9). ESI(+)-HRMS: (m/z) calcd. for $[C_{12}H_6N_2F_2O+H]^+$ = 233.0524; found: 233.0521.

2.6. General Procedure for the Synthesis of 2,9-Dihalogenated Phenanthroline Epoxides (Cl, Br, I)

The 2,9-dihalogenated phenanthrolines were dissolved in chloroform, and tetrabutylammonium hydrogensulfate (250 mg, 0.74 mmol) was added to the mixture. The suspension was sonicated until everything had dissolved. The experiments were conducted with commercial bleach (Dan Klorix, 2–5% active chlorine), and 500 mL of bleach was used. In a separate beaker, the pH of the bleach solution was carefully adjusted to 8.6 using concen-

trated sulfuric acid before adding it to the reaction mixture. Both solutions were combined and stirred vigorously for 24 h. The pH of the solutions was monitored over the course of the reaction and adjusted back to 8.6 if it fell below 8.2. The reactions were monitored via NMR. This was done by taking a small aliquot of the reaction solution and extracting it with $CDCl_3$ to monitor the growing signal of the protons in the 5,6-position with a chemical shift between 4 and 5 ppm. The reaction was stopped, and saturated Na_2CO_3 solution (100 mL) was added to the solution. Then the mixture was extracted with DCM (5 × 50 mL). The combined organic layers were washed with water (100 mL) and a saturated Na_2CO_3 solution (3·75 mL) to remove the phase transfer catalyst. The organic layer was dried over $MgSO_4$, and the products were purified via flash column chromatography (silica gel). In many cases, more than one column was required to obtain a sufficiently pure product, as starting material and product have similar properties. Conversion was usually around 10–50%. The remaining starting material can be recovered by column chromatography and recycled.

*2.7. 5,6-Epoxy-5,6-dihydro-2,9-dichloro-[1,10]phenanthroline (**8**)*

The reaction was conducted as described in the general procedure 2.2. 2,9-dichloro-[1,10]phenanthroline (**3**) (0.350 g, 1.42 mmol, 1.00 eq.) was added as a solution in $CHCl_3$ (50 mL), and tetrabutylammonium hydrogensulfate (250 mg, 0.74 mmol, 0.52 eq.) was added. After 24 h, the reaction was stopped, and the white solid obtained after extraction was purified via flash column chromatography (silica gel, DCM/acetone 100:1 → 80:1, R_f = 0.49 (DCM/acetone 100:1)). The product was obtained as a white solid (0.198 g, 0.752 mmol, 53%). ^{1}H NMR: (400 MHz, DMSO-d_6, ppm) δ = 8.34 (d, $^3J_{HH}$ = 8.1 Hz, 2H, H4, H7), 7.68 (d, $^3J_{HH}$ = 8.1 Hz, 2H, H3, H8), 4.89 (s, 2H, H5, H6). ^{13}C{^{1}H} NMR: (101 MHz, DMSO-d_6, ppm) δ = 151.3 (C2, C9), 148.3 (C10a, C10b), 142.5 (C4, C7), 129.9 (C4a, C6a), 125.5 (C3, C8), 54.2 (C5, C6). ^{15}N{^{1}H} NMR: (40 MHz, DMSO-d_6, ppm) δ = 302 (N1, N10). ESI(+)-HRMS (*m*/*z*): calcd. for $[C_{12}H_6N_2Cl_2O+H]^+$ = 264.9933, found: 264.9935. Elemental analysis calcd. for $C_{12}H_6N_2Cl_2O$: C 54.4; H 2.3; N 10.6, found: C 54.3; H 2.4; N 10.5.

*2.8. 5,6-Epoxy-5,6-dihydro-2,9-dibromo-[1,10]phenanthroline (**9**)*

The reaction was conducted as described in the general procedure 2.2. The 2,9-dibromo-[1,10]phenanthroline (**4**) (0.835 g, 2.36 mmol, 1.00 eq.) was added as a solution in $CHCl_3$ (50 mL), and tetrabutylammonium hydrogensulfate (250 mg, 0.74 mmol, 0.31 eq.) was added. After 24 h, the reaction was stopped, and the white solid obtained after extraction was purified via flash column chromatography (silica gel, DCM/acetone 100:1 → 80:1, R_f = 0.51 (DCM/acetone 100:1)). The product was obtained as a white solid (0.294 g, 0.835 mmol, 35%). ^{1}H NMR: (400 MHz, DMSO-d_6, ppm) δ = 8.26 (d, $^3J_{HH}$ = 8.0 Hz, 2H, H4, H7), 7.85 (d, $^3J_{HH}$ = 8.0 Hz, 2H, H3, H8), 4.90 (s, 2H, H5, H6). ^{13}C{^{1}H} NMR: (101 MHz, DMSO-d_6, ppm) δ = 149.0 (C10a, C10b), 142.6 (C2, C9), 142.4 (C4, C7), 130.6 (C4a, C6a), 129.5 (C3, C8), 54.5 (C5, C6). ^{15}N{^{1}H} NMR: (40 MHz, DMSO-d_6, ppm) δ = 311 (N1, N10). ESI(+)-HRMS (*m*/*z*): calcd. for $[C_{12}H_6N_2Br_2O+Na]^+$= 374.8744, found: 374.8745. Elemental analysis calcd. for $C_{12}H_6N_2Br_2O$: C 40.7; H 1.7; N 7.9, found: C 40.7; H 1.80; N 7.9.

*2.9. 5,6-Epoxy-5,6-dihydro-2,9-diiodo-[1,10]phenanthroline (**10**)*

The reaction was conducted as described in the general procedure 2.2. The 2,9-diiodo-[1,10]phenanthroline (**5**) (1.10 g, 2.55 mmol, 1.00 eq.) was added as a solution in $CHCl_3$ (60 mL), and tetrabutylammonium hydrogensulfate (250 mg, 0.74 mmol, 0.29 eq.) was added. After 24 h, the reaction was stopped, and the white solid obtained after extraction was purified via flash column chromatography (silica gel, DCM/acetone 100:1 → 80:1, R_f = 0.51 (DCM/acetone 100:1)). The product was obtained as a white solid (0.264 g, 0.592 mmol, 23%). ^{1}H NMR: (400 MHz, DMSO-d_6, ppm) δ = 8.03 (d, $^3J_{HH}$ = 8.0 Hz, 2H, H3,

H8), 7.98 (d, $^{3}J_{HH}$ = 8.0 Hz, 2H, H4, H7), 4.85 (s, 2H, H5, H6). $^{13}C\{^{1}H\}$ NMR: (101 MHz, DMSO-d_6, ppm) δ = 149.6 (C10a, C10b), 141.0 (C4, C7), 136.0 (C3, C8), 130.5 (C4a, C6a), 120.1 (C2, C9), 54.7 (C5, C6). $^{15}N\{^{1}H\}$ NMR: (40 MHz, DMSO-d_6, ppm) δ = 325 (N1, N10). ESI(+)-HRMS (m/z): calcd. for $[C_{12}H_6N_2I_2O+Na]^+$ = 470.8462, found: 470.8457. Elemental analysis calcd. for $C_{12}H_6N_2I_2O$: C 32.2; H 1.4; N 6.3, found: C 32.2; H 1.5; N 6.1.

2.10. X-Ray

Intensity data were collected using monochromated MoKα radiation on a Bruker D8 Venture diffractometer with a Photon III detector using the APEX6 software suite [20–22]. The collection method involved ω scans. Data reduction was performed using the program *SAINT* (Version V8.42) [21]. The crystal structures were solved by Intrinsic Phasing using *SHELXT* (Version 2018/2) [22]. Non-hydrogen atoms were first refined isotropically, followed by anisotropic refinement by full-matrix least-squares calculation based on F^2 using *SHELXL* (Version 2019/2) [23]. H atoms were located on the electron density map and then positioned geometrically and allowed to ride on their respective parent atoms, except for compound **6 · H$_2$O**, where the H atoms of the water molecules were refined independently. The structure of **6 · H$_2$O** can be solved in *Pc* [R(int) = 0.0416; R1 = 0.0553; wR2 = 0.1477)], and in *P*1 [R(int) = 0.021]. A Flack parameter of 0.5(16) suggested the presence of an inversion twin. An alternative solution in *P*–1 was not possible. The systematic extinctions in the raw data were mostly, but not completely fulfilled, suggesting space group *Pc*. However, analysis with Jana [24] suggested twinning and transformation from *Pc* to the translationengleiche subgroup *P*1 as the best solution.

Further details of the crystal structure determinations are available from the Cambridge Crystallographic Data Centre by quoting the depository number CCDC 2571043-2571050. Table 1 with the crystallographic details was created using *FinalCif* [25]. The molecular structures were visualized and analyzed using the Diamond 5.0.0 software [26]. For the Hirshfeld analysis and surface plots, CrystalExplorer 21.5 (Revision 608bb32) was used [27]. The close-packing indices (CP_i) were determined based on the van der Waals surface volumes and Hirshfeld surface volumes of the molecules in the crystal structure (Table S1) [28]. In addition, the Kitaigorodskii packing indices (KPI) were determined using the PLATON software (Version 51222) [29].

Table 1. Crystallographic data of compounds **2**, **5**, **6–10**.

	2	**5**	**6**	**6 · H_2O**	**7**	**8**	**9**	**10**
CCDC	2571048	2571044	2571050	2571047	2571043	2571046	2571045	2571049
Empirical formula	$C_{12}H_6F_2N_2$	$C_{12}H_6I_2N_2$	$C_{12}H_8N_2O$	$C_{12}H_{10}N_2O_2$	$C_{12}H_6F_2N_2O$	$C_{12}H_6Cl_2N_2O$	$C_{12}H_6Br_2N_2O$	$C_{12}H_6I_2N_2O$
Formula weight	216.19	431.99	196.20	214.22	232.19	265.09	354.01	447.99
Crystal system	Monoclinic	Monoclinic	Orthorhombic	Triclinic	Orthorhombic	Orthorhombic	Orthorhombic	Orthorhombic
Space group	$P2_1/n$	$P2_1/n$	*P*bca	*P*1	$Pca2_1$	$P2_12_12_1$	$P2_12_12_1$	$P2_12_12_1$
a, Å	7.3753(7)	12.2796(3)	12.7528(2)	4.9417(3)	16.5371(16)	4.4979(8)	4.5981(3)	4.73510(9)
b, Å	10.3362(12)	14.7128(4)	7.83660(10)	7.5181(5)	4.4684(4)	12.015(2)	12.1746(9)	12.5360(2)
c, Å	11.8249(14)	13.3021(3)	17.6336(3)	13.1585(8)	12.8315(13)	19.534(3)	19.6145(15)	19.8908(4)
α, deg.	90	90	90	90.507(2)	90	90	90	90
β, deg.	94.525(5)	100.9220(10)	90	90.014(2)	90	90	90	90
γ, deg.	90	90	90	99.932(2)	90	90	90	90
V, $Å^3$	898.63(17)	2359.72(10)	1762.28(5)	481.52(5)	948.18(16)	1055.7(3)	1098.02(14)	1180.70(4)
Z	4	8	8	2	4	4	4	4
ρ_{calc}, g cm^{-3}	1.598	2.432	1.479	1.477	1.627	1.668	2.141	2.520
μ(MoKα), mm^{-1}	0.126	5.303	0.097	0.103	0.133	0.595	7.364	5.310
Crystal size, mm^3	0.05 × 0.10 × 0.13	0.08 × 0.07 × 0.05	0.11 × 0.08 × 0.04	0.16 × 0.04 × 0.02	0.11 × 0.11 × 0.01	0.39 × 0.02 × 0.02	0.26 × 0.02 × 0.01	0.11 × 0.10 × 0.04
Temperature (K)	115(2)	100(2)	100(2)	100(2)	120(2)	100(2)	100(2)	100(2)
θ range, deg.	2.62–27.87	2.491–33.161	2.809–30.105	2.751–28.721	2.463–27.095	2.085–30.170	2.077–30.098	2.614–30.022
hkl range, deg.	−9:9, −13:13, −15:15	−18:18, −22:22, −20:20	−17:17, −11:11, −24:24	−6:6, −10:10, −17:17	−21:21, −5:5, −16:16	−6:6, −16:16, −27:27	−6:6, −17:17, −27:27	−6:6, −17:17, −28:28
Total/unique data/R_{int}	12,718/2144/ 0.0523	50,857/9007/ 0.0236	30,563/2583/ 0.0343	7532/4832/ 0.0212	10,112/2091/ 0.0563	11,100/3115/ 0.0625	17,722/3239/ 0.0551	20,407/3450/ 0.0234
Data/restraints/parameters	2144/0/145	9007/0/289	2583/0/136	4832/3/305	2091/1/154	3115/0/154	3239/0/154	3450/0/154
R_1/wR_2 [$I > 2\sigma(I)$]	0.0453/0.1229	0.0166/0.0374	0.0437/0.1139	0.0472/0.1148	0.0566/0.0924	0.0478/0.1215	0.0275/0.0662	0.0110/0.0289
R_1/wR_2 [all data]	0.0534/0.1302	0.0183/0.0380	0.0469/0.1163	0.0552/0.1200	0.0802/0.0987	0.0521/0.1245	0.0306/0.0675	0.0112/0.0290
Flack parameter	n/a	n/a	n/a	0.0(7)	0.1(5)	0.00(6)	−0.003(8)	−0.037(9)
S	1.068	1.079	1.051	1.068	1.102	1.040	1.030	1.127
Min./max. res. dens., $eÅ^{-3}$	0.37/−0.29	0.61/−1.04	0.45/−0.24	0.35/−0.23	0.22/−0.23	0.61/−0.32	0.85/−0.76	0.37/−0.40

2.11. Cell Viability

Cell viability was determined by the MTT (3-(4,5-dimethylthiazol-2-yl)-2,5-diphenyltet razolium bromide) assay [30] in the non-tumorigenic Vero cell line (African green monkey kidney cells) as well as in the human cancer cell lines HepG2 (hepatocellular carcinoma), A549 (lung carcinoma) and A498 (kidney carcinoma). Cells were cultured in DMEM medium, except for Vero cells, which were maintained in RPMI medium (PAN-Biotech, Aidenbach, Germany), supplemented with 10% fetal calf serum (FCS; Sigma-Aldrich, Burlington, MA, USA) and penicillin/streptomycin (100 U/mL; Sigma-Aldrich, Burlington, MA, USA) and maintained at 37 °C/10% CO_2 in 75 cm^2 culture flasks (Sarstedt, Germany). Cells were seeded at a density of 2.0×10^5 cells/mL (Vero), 1.2×10^5 cells/mL (HepG2, A498) or 8.0×10^4 cells/mL (A549) in 96-well plates (Sarstedt, Numbrecht, Germany). Cell counting was performed using a CASY Cell Counter and Analyzer (Schärfe System, Reutlingen, Germany). After 24 h, cells were washed with phosphate-buffered saline (PBS), and 100 µL of the respective test solutions in culture medium were added. Compounds **1** to **10** were assayed at concentrations ranging from 0.1 to 500 µM. Disodium ethylenediaminetetraacetate (Na_2EDTA, AppliChem, Darmstadt, Germany) was included for comparison. Paclitaxel or camptothecin (Sigma-Aldrich, Burlington, MA, USA) was used as a positive control, depending on the susceptibility of the cell line, and was assayed in a concentration range of 0.0001 to 10 µM. As DMSO was used for solubilization, culture medium containing $\leq$0.5% DMSO was used as a negative control. Further, a growth control (culture medium supplemented with 10% FCS) was included. After another 48 h of incubation, cells were washed twice in PBS, and 50 µL of MTT reagent (0.5 mg/mL) in culture medium was added. After 4 h, the MTT solution was replaced with 50 µL DMSO, and after agitation for 10 min, the absorbance was measured at 595 nm using a microtiter plate reader (Tecan Spark, Tecan, Männedorf, Switzerland). Dose–response curves including the half maximal inhibitory concentration related to the negative control (IC_{50} values) were calculated by non-linear regression using GraphPad Prism (Version 11 for Windows; GraphPad Software, Boston, MA, USA). Results are displayed as mean and standard error (SEM) from $\geq$3 independent experiments with at least three technical replicates.

2.12. Antibacterial Assays

All assays were performed using *P. aeruginosa* ATCC 27853. Bacteria were cultured on LB agar (25 g/L lysogeny broth, 15 g/L agar-agar, Carl Roth). Minimum inhibitory concentrations (MIC) were assessed as described previously [31]. Briefly, liquid cultures from single colonies were grown at 37 °C in cation-adjusted Mueller–Hinton broth (CAMHB; Sigma-Aldrich, USA) to a concentration of approx. 10^8 CFU/mL. A 1:100 dilution of this suspension was subsequently used for the assays. Compounds **1** to **10** were solubilized in DMSO and assayed in 96-well plates (Standard R, Sarstedt, Germany) in serial dilutions from 256 to 0.5 µM (approx. 114 to 0.1 µg/mL) in CAMHB. Liquid medium containing 0.5% DMSO was used as a negative control; gentamicin (8–0.5 µg/mL; Sigma-Aldrich, USA) was used as a positive control. Additionally, sterile controls and blanks containing only the test solution were included. After 20 h incubation at 37 °C, the MICs were determined as the lowest concentrations showing no visible bacterial growth.

The formation of biofilms was quantified by crystal violet staining [32]. Bacteria were incubated overnight as described for the growth assays. After removal of the bacterial suspension, biofilms were rinsed twice in water (Synergy UV, Merck Millipore, Darmstadt, Germany), dried for 1 h and stained with 200 µL crystal violet solution (0.1% in water; Merck, Darmstadt, Germany). The staining solution was removed after 10 min, followed by another rinsing step and drying for 2 h. Biofilms were dissolved in 200 µL acetic acid (30%, *v*/*v*); 125 µL was transferred to a flat-bottomed 96-well plate, and the absorbance was

measured at 550 nm using a microtiter plate reader. In addition to the standard conditions, the experiments were also performed in Vogel–Bonner minimal medium using plasticware to limit the concentration of trace metals. Antibacterial assays were performed in three independent experiments, including at least three technical replicates. The results of the biofilm assay were summarized as bar charts using GraphPad Prism.

3. Results

3.1. Synthesis of Dihalogenated Phenanthroline Derivatives and Epoxides

1,10-Phenanthroline (**1**), as well as the dichlorinated and dibrominated 1,10-phenanthro line derivatives **3** and **4**, were obtained from commercial sources. The difluorinated compound **2** was synthesized starting from 2,9-dichloro-1,10-phenanthroline (**3**) (Scheme 1). To this end, compound **3** was reacted with cesium fluoride in the presence of a crown ether, enabling halogen exchange and replacement of the chlorine substituents with fluorine atoms. Following chromatographic purification, the difluorinated product **2** was isolated in excellent yield (93%). The diiodinated derivative **5** was prepared by direct conversion of the chlorinated precursor **3** using aqueous hydroiodic acid (Scheme 1). After recrystallization, compound **5** was obtained in good yield (72%). The isolated single crystals were suitable for X-ray crystallographic analysis.

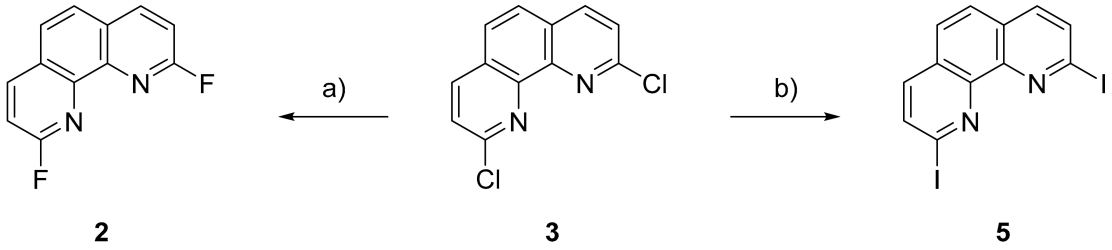

2 **3** **5**

Scheme 1. Synthesis of the dihalogenated 1,10-phenanthroline derivatives: (a) 0.15 eq. $(CH_3)_4NCl$, 0.15 eq. 18-crown-6, 6.0 eq. CsF, DMSO, 100 °C, 4.5 h, 93%; (b) HI, 105 °C, 72 h, 72%.

The epoxidation of 1,10-phenanthroline (**1**) was carried out using commercial bleach in the presence of tetrabutylammonium hydrogensulfate (Scheme 2). Regular monitoring and adjustment of the pH of the reaction mixture within a narrow range of 8.6–8.2 proved essential for the success of the transformation. pH values below 8.2 preferentially led to the formation of chlorinated side products. After chromatographic purification, compound **6** was isolated in excellent yield (94%). Epoxidation of the difluorinated derivative **2** was performed with potassium bromate in sulfuric acid at room temperature. Subsequent chromatographic purification afforded compound **7** in very good yield (86%). The epoxidation of the remaining dihalogenated derivatives **3**–**5** was achieved in analogy to the non-halogenated parent compound using commercial bleach as the oxidant. The pH was likewise maintained between 8.6 and 8.2 throughout the course of the reaction. However, compared with the non-halogenated substrate, substantially longer reaction times were necessary to achieve satisfactory conversion. Nevertheless, the yields were low because, in some cases, more than one purification step by chromatography was necessary.

3.2. Molecular Structures and Supramolecular Features of the Phenanthroline Derivatives **2** *and* **5**

2,9-Difluoro-1,10-phenanthroline **2** crystallizes in the space group $P2_1/n$, with one molecule in the asymmetric unit (Figure 1A). The packing diagram shows that the molecules form curved, laminar layers (Figure 1B). In this arrangement, the molecules interact with other molecules along the molecular plane via short H···F contacts (short-contact geometries: C2–H2···F2′, d(D–H) = 0.95 Å, d(H···A) = 2.43 Å, d(D···A) = 3.219(2) Å, ∠(DHA) = 140.8°, A = F2′; and C5–H5···F1′, d(D–H) = 0.95 Å, d(H···A) = 2.44 Å, d(D···A) =

3.373(2) Å, ∠(DHA) = 167.7°, A = F1′, symmetry operation: (′) 0.5 + x, 1.5 − y, 0.5 + z). It is notable that, perpendicular to the molecular plane, two molecules always stack on top of one another with a slight offset (interplanar distance 3.34 Å).

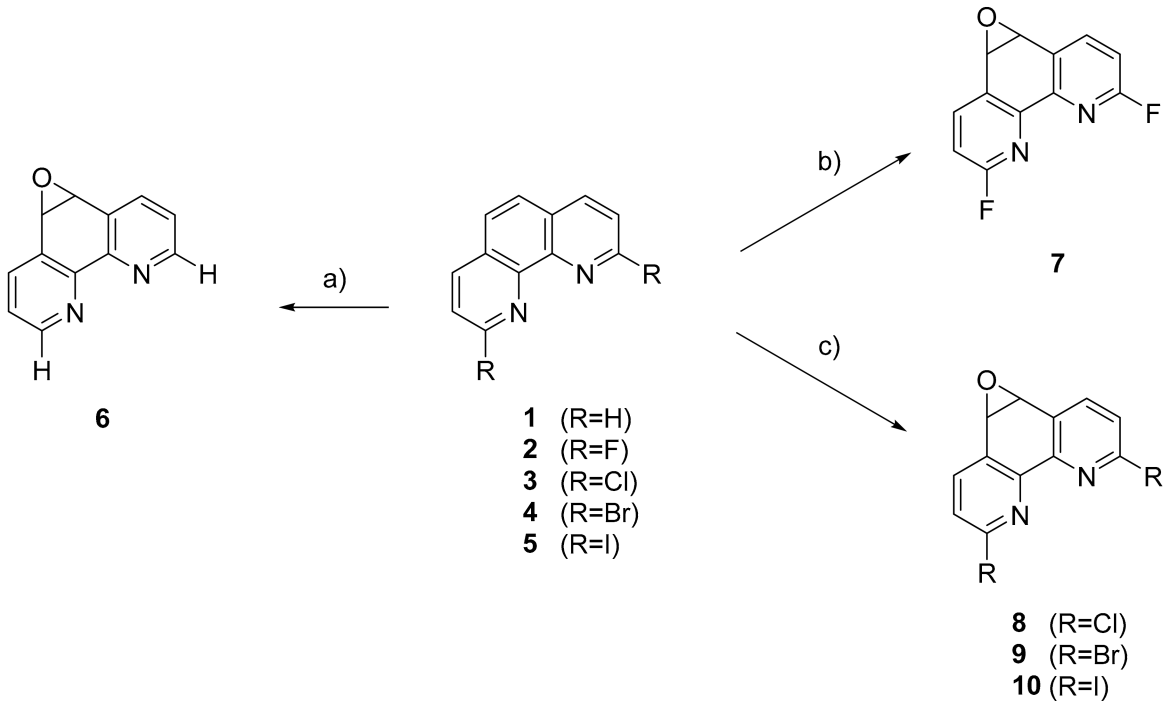

Scheme 2. Synthesis of 1,10-phenanthroline epoxide derivatives: (a) $^{n}Bu_4NHSO_4$, Dan Klorix, $CHCl_3$, rt, 75 min, 94%; (b) $KBrO_3$, H_2SO_4, rt, 16 h, 86%; (c) $^{n}Bu_4NHSO_4$, Dan Klorix, $CHCl_3$, rt, 24 h, 23201353%.

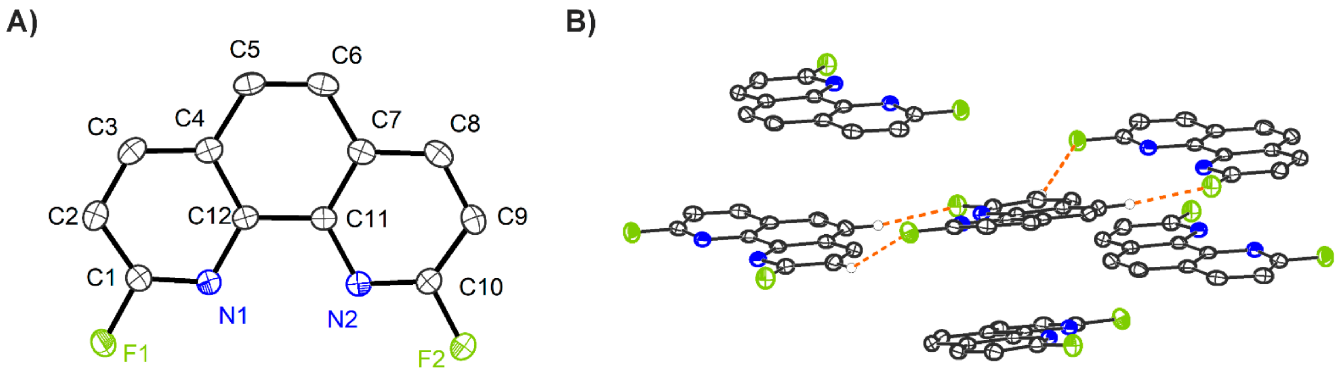

Figure 1. (A) Molecular structure of compound **2**. (B) Partial packing diagram with highlighted short contacts of compound **2**. (Displacement ellipsoids are shown at the 50% level; hydrogen atoms are omitted for clarity, except for selected atoms in (B). Color coding: H: ○, C: ⊕, N: ●, F: ●).

2,9-Diiodo-1,10-phenanthroline **5** crystallizes in the space group $P2_1/n$, with two independent molecules in the asymmetric unit (Figure 2A). Although the individual molecules within the asymmetric unit exhibit a stacking arrangement, they are not coplanar (interplanar angle ~18°). The overall molecular packing in the crystal structure resembles a sandwich-herringbone motif (Figure 2B) [33]. Within this packing arrangement, the molecules interact predominantly through short intermolecular contacts between the iodine atoms, with I···I distances of 3.7455(4) Å and 3.9265(4) Å [34,35]. The sandwich structure is stabilized via stacking interactions [36] and additional C–H···I interactions [37,38] mediate between the stacks. Overall, this crystal structure differs markedly from those of

the corresponding chlorinated and brominated derivatives. Here, the molecules adopt a herringbone arrangement without any significant short contacts between the respective halogen substituents [39,40].

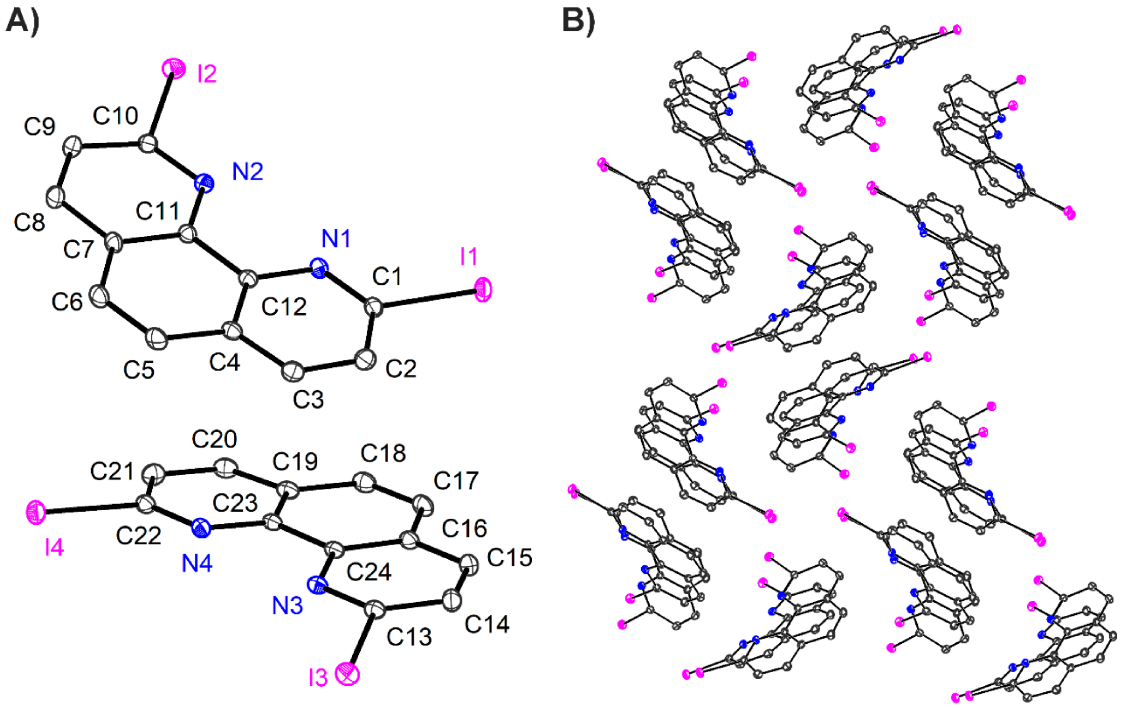

Figure 2. (A) Molecular structure of compound **5**. (B) Partial packing diagram of compound **5**. (Displacement ellipsoids are shown at the 50% level; hydrogen atoms are omitted for clarity. Color coding: C: ⊕, N: ●, I: ●).

3.3. Molecular Structures of the Phenanthroline Epoxides

The 1,10-phenanthroline epoxides **6**–**10** crystallize in one of the orthorhombic space groups *Pbca*, $Pca2_1$, and $P2_12_12_1$, each with one molecule in the asymmetric unit (Figure 3A–E). Despite the two stereocenters at the carbon atoms of the epoxide, compounds **6**–**10** are *meso-cis* isomers due to the present mirror plane (Figure 3F). In all cases, the phenanthroline scaffold is planar, while the three-membered epoxide ring is inclined relative to the phenanthroline plane, with interplanar angles of 100.8(1)° to 104.01(5)°.

In addition to the crystal structures of the isolated molecules, a monohydrate structure of the 1,10-phenanthroline epoxide was obtained. This compound crystallizes in space group *P*1, with two 1,10-phenanthroline epoxide molecules and two water molecules in the asymmetric unit. The water molecules are stabilized in the crystal structure through hydrogen-bonding interactions with the phenanthroline units. In each case, one hydrogen atom of each water molecule interacts with both nitrogen atoms of a phenanthroline epoxide molecule (Figure 4A).

Furthermore, the water molecules form an extended hydrogen-bonding network (hydrogen-bond geometries: O4–H1C···O3, d(D–H) = 0.84(6) Å, d(H···A) = 2.02(6) Å, d(D···A) = 2.860(4) Å, ∠(DHA) = 178(5)°, A = O3; and O3–H1B···O4′, d(D–H) = 0.82(6) Å, d(H···A) = 2.05(6) Å, d(D···A) = 2.875(4) Å, ∠(DHA) = 176(5)°, A = O4′, symmetry operation: (′) 1 + x, y, z). This network connects the individual phenanthroline units to one another within the crystal packing (Figure 4B, Table 2).

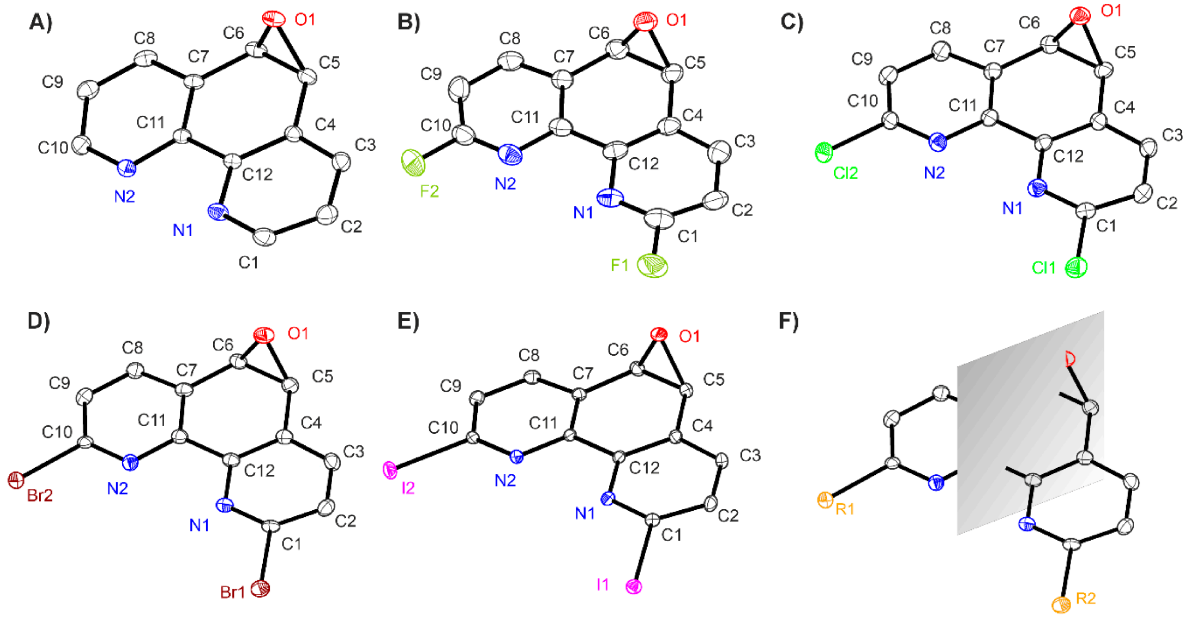

Figure 3. Molecular structures of compound **6** (A), compound **7** (B), compound **8** (C), compound **9** (D), compound **10** (E), and highlighted mirror plane of the epoxides with arbitrary residues R1 and R2 (F). (Displacement ellipsoids are shown at the 50% level; hydrogen atoms are omitted for clarity. Color coding: C: ⊕, N: ●, O: ●, F: ●, Cl: ●, Br: ●, I: ●).

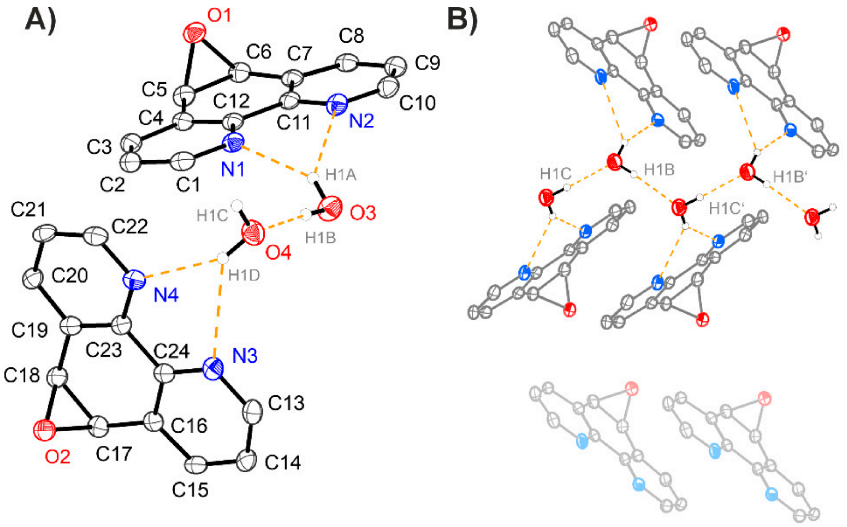

Figure 4. (A) Asymmetric unit of compound **6 · H_2O** with highlighted hydrogen-bonding interactions. (B) Partial packing diagram of compound **6 · H_2O** with highlighted hydrogen-bonding interactions (symmetry code: (′) 1 − x, 1 − y, 1 − z). (Displacement ellipsoids are shown at the 50% level; hydrogen atoms except for the water protons (arbitrary radius of 0.135 Å) are omitted for clarity. Color coding: H: ○, C: ⊕, N: ●, O: ●).

Table 2. Overview of the hydrogen-bonding interactions in the asymmetric unit of compound **6 · H_2O**.

Hydrogen Bond	d(D–H)/Å	d(H···A)/Å	d(D···A)/Å	∠(DHA)/°
O3–H1A···N2	0.87(6)	2.62(6)	3.308(4)	136(5)
O3–H1A···N1	0.87(6)	2.17(6)	2.976(4)	153(4)
O4–H1D···N4	0.95(6)	2.16(6)	2.985(4)	146(4)
O4–H1D···N3	0.95(6)	2.54(6)	3.321(4)	140(4)

3.4. Supramolecular Features of the Phenanthroline Epoxides

The intermolecular interactions of the epoxides are governed by stacking interactions between the phenanthroline units, as well as by contacts between heteroatoms and hydrogen atoms. In the case of 1,10-phenanthroline epoxide **6**, the molecules assemble, among other motifs, in such a way that the epoxide moieties are on opposite sides of the respective molecular planes (Figure 5A). The distance between the two molecular planes is 3.36 Å, which is within the range typically observed for comparable stacking interactions [36,41]. In addition, two hydrogen-bonding interactions involving the oxygen atom of the epoxide connect the molecules in the solid state. One originates from the oxirane protons of an adjacent epoxide unit (hydrogen-bond geometry: C5–H5···O1′, *d*(D–H) = 1.00 Å, *d*(H···A) = 2.33 Å, *d*(D···A) = 3.2813(14) Å, ∠(DHA) = 159°, A = O1′, symmetry operation: (′) −x + 3/2, y + 1/2, z), while the other arises from an adjacent C–H bond of a second molecule (hydrogen-bond geometry: C2–H2···O1′, *d*(D–H) = 0.95 Å, *d*(H···A) = 2.54 Å, *d*(D···A) = 3.4245(14) Å, ∠(DHA) = 156°, A = O1′, symmetry operation: (′) −x + 1, y + 1/2, −z + 1/2).

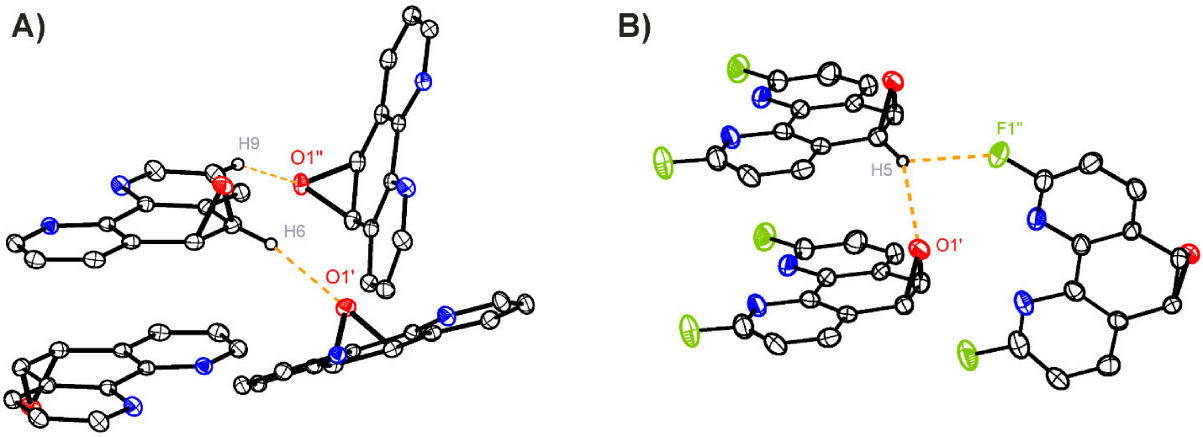

Figure 5. (A) Partial packing diagram of compound **6** with highlighted short contacts (symmetry codes: (′) −x + 3/2, y + 1/2, z; (″) −x + 1, y + 1/2, −z + 1/2). (B) Partial packing diagram of compound **7** with highlighted short contacts (symmetry codes: (′) x, −1 + y, z; (″) 1/2 − x, −1 + y, 1/2 + z). (Displacement ellipsoids are shown at the 50% level; hydrogen atoms are omitted for clarity. Color coding: H: ○, C: ⊕, N: ●, O: ●, F: ●).

The molecules of the fluorinated derivative **7** also exhibit stacking interactions. In this case, the molecules are arranged in a head-to-head orientation, resulting in the epoxide rings pointing in the same direction (Figure 5B). The interplanar distance of 3.51 Å is larger than that observed for the unsubstituted phenanthroline epoxide **6**, which may be associated with the orientation of the oxirane rings. Due to the orientation of the oxirane rings, an additional hydrogen-bonding interaction between the oxirane protons of one epoxide unit and the oxygen atom of an adjacent epoxide is formed (hydrogen-bond geometry: C6–H6···O1′, *d*(D–H) = 1.00 Å, *d*(H···A) = 2.36 Å, *d*(D···A) = 3.230(6) Å, ∠(DHA) = 145°, A = O1′, symmetry operation: (′) x, −1 + y, z). Furthermore, a short contact is observed between an oxirane C–H bond and a fluorine atom (short-contact geometry: C6–H6···F1′, *d*(D–H) = 1.00 Å, *d*(H···A) = 2.43 Å, *d*(D···A) = 3.092(5) Å, ∠(DHA) = 123°, A = F1′, symmetry operation: (′) 1/2 − x, −1 + y, 1/2 +z).

The crystal structures obtained for the halogenated derivatives **8**, **9** and **10** are isotypic and exhibit intermolecular interactions with several common features (Figure 6). Interestingly, in the case of the iodinated compound **10**, the enantiomorph of the other two crystal structures was obtained. In all structures, the phenanthroline units stack on top of each

other with only a small displacement, with epoxide moieties oriented in the same direction and a head-to-head arrangement of the molecules.

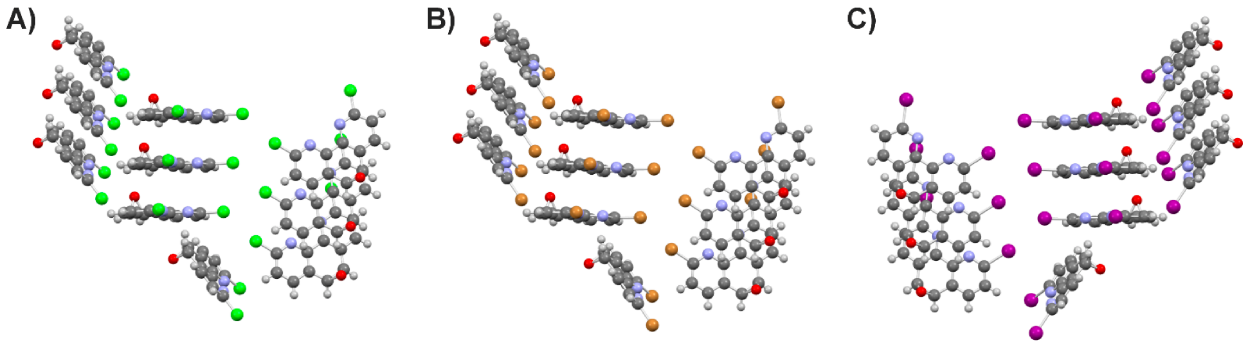

Figure 6. Partial packing diagrams of compound **8** (A), compound **9** (B), and compound **10** (C) highlighting the isotypic character of these structures. (Ball-and-stick representation at arbitrary radii). Color coding: H: ○, C: ⊕, N: ●, O: ●, Cl: ●, Br: ●, I: ●).

The intermolecular interactions of epoxides **8**, **9**, and **10** differ significantly from those of the compounds described so far. As the atomic number of the halogen substituents increases, the electronic properties change significantly, leading to the formation of different interactions. While in the fluorinated derivative **7**, interactions between adjacent halogen atoms and oxygen atoms of stacked epoxides are formed by a single oxirane proton (Figure 5B), analogous interactions are formed independently by both oxirane protons, already visible in the chlorinated compound **8** (Figure 7A, Table 3).

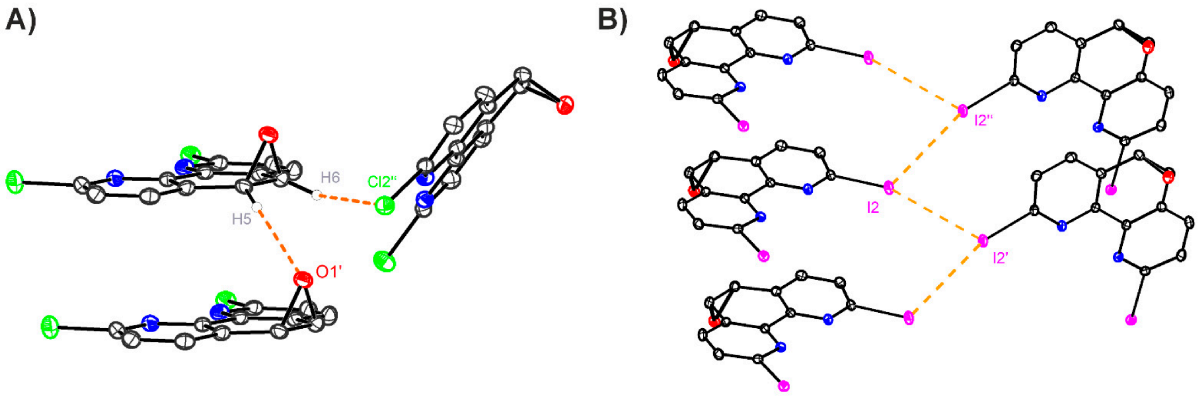

Figure 7. (A) Partial packing diagram of compound **8** with highlighted short contacts (symmetry codes: (′) 1 + x, y, z; (″) 1 − x, 1/2 + y, 1/2 − z). (B) Partial packing diagram of compound **10** with highlighted short contacts (symmetry codes: (′) x, 1 + y, z; (″) 3/2 − x, 1 + y, −1/2 + z). (Displacement ellipsoids are shown at the 50% level; hydrogen atoms are omitted for clarity. Color coding: H: ○, C: ⊕, N: ●, O: ●, Cl: ●, I: ●).

The hydrogen bond in the fluorinated compound **7** can still be classified as a moderately strong hydrogen bond according to *Steiner* due to the short-contact distances [42], but in the case of the chlorinated, brominated, and iodinated compounds, these interactions are merely weak due to the larger distances between involved atoms. Due to the stronger interactions and the resulting shorter distances in compound **7**, the phenanthroline units cannot stack as closely along the direction perpendicular to their molecular planes because of steric repulsion with the epoxide ring. Nevertheless, the stacked molecules of compound **7** are arranged almost directly on top of each other, with only a slight offset of one six-membered ring. In contrast, the derivatives with heavier halogen substituents **8**, **9** and

10 adopt a more laterally displaced stacking arrangement, resulting in shorter distances between the phenanthroline planes (3.33 Å–3.39 Å).

Table 3. Overview of the hydrogen-bonding interactions and selected short contacts in the solid-state structures of derivatives **8**, **9** and **10** (symmetry codes: (′) 1/2 + x, 3/2 − y, 1 − z; (″) 1 + x, y, z; (‴) 1 − x, 1/2 + y, 1/2 – z, (⁗) -1/2 + x, 1/2 − y, 1 − z; (⁗′) -1 + x, y, z; (⁗″) 1 − x, -1/2 + y, 3/2 − z).

Hydrogen Bond	Cmpd	d(D–H)/Å	d(H···A)/Å	d(D···A)/Å	∠(DHA)/°
C2–H2···O1′	**8**	0.95	2.64	3.203(4)	118.1
C2–H2···O1′	**9**	0.95	2.61	3.195(4)	120.6
C9–H9···O1⁗	**10**	0.95	2.61	3.252(3)	125.2
Short Contact	Cmpd	d(D–H)/Å	d(H···A)/Å	d(D···A)/Å	∠(DHA)/°
C5–H5···O1″	**8**	1.00	2.61	3.577(5)	161.8
C5–H5···O1″	**9**	1.00	2.71	3.679(5)	163.8
C6–H6···O1⁗′	**10**	1.00	2.85	3.830(3)	165.1
Short Contact	Cmpd	d(D–H)/Å	d(H···A)/Å	d(D···A)/Å	∠(DHA)/°
C6–H6···Cl2‴	**8**	1.00	2.81	3.559(3)	131.9
C6–H6···Br2‴	**9**	1.00	2.93	3.670(4)	132.0
C5–H5···I1⁗″	**10**	1.00	3.08	3.830(2)	132.6

The aromatic protons form hydrogen-bonding interactions with an adjacent epoxide unit and establish short contacts with an adjacent halogen atom of another molecule (Table 3). While the donor–acceptor distances associated with the hydrogen-bonding interactions change only slightly as a function of the halogen substituent, and the corresponding angles vary only marginally, a different trend is observed for the short contacts between the oxirane protons and the halogen atoms or oxygen atoms of adjacent epoxides. While the contact angles remain nearly unchanged, the corresponding distances increase considerably for the heavier halogen atoms (Table 3). In case of the brominated epoxide **9** and the iodinated epoxide **10**, additional halogen···halogen interactions are observed (Br1···Br1′: 3.6221(6) Å, symmetry operation: (′) 1/2 + x, 1/2 − y, 1 − z; I2···I2′: 3.8312(4) Å, symmetry operation: (′) 1/2 + x, 3/2 − y, 1 − z). These contacts propagate through the crystal structure in a stepwise fashion, thereby linking the molecules into an extended network-like arrangement. The shortest halogen···halogen distance in compound **8** (3.519(1) Å) is larger than the sum of the van der Waals radii of the chlorine atoms, indicating no significant interaction.

3.5. Hirshfeld Surface Analysis

Hirshfeld surface plots are well-established representations for providing a condensed summary of intermolecular interactions [43]. They can be used to identify short-range contacts between nuclei of one molecule and nuclei of another, which are highlighted by red areas on the d_{norm} surface. In the case of the unsubstituted 1,10-phenanthroline epoxide **6**, a strong interaction occurs via the nitrogen atoms (Figure 8A, point i), an interaction that is less pronounced in the halogenated derivatives. The interaction via the oxygen atom of the epoxide (Figure 8A, point ii) is present in all cases, but the intensity of this interaction decreases in the halogenated derivatives. With the introduction of a fluorine atom, an interaction via the halogen substituents becomes possible (Figure 8B, point iii), which increases further with the atomic number of the halogen atom (Figure 8C, point iv). The fact that compound **10** is the enantiomorph of compounds **8** and **9** can also be seen from the Hirshfeld plots as the strong interactions via the halogen atoms shift to the other side of the molecule (Figure 8E, point v). The interactions can further be quantified using the fingerprint plots (Figures S18–S22) of the respective elements (Figure 8F). When comparing

selected interactions of the individual compounds with each other, it becomes apparent that the intermolecular interactions of compound **6** are dominated by a large number of H···H contacts (Figure 8F). In compounds **7**–**10**, this contribution is greatly reduced due to the presence of X···H interactions. The proportions of O···H and N···H contacts decrease steadily with halogenation and as the atomic number of the halogens increases. Furthermore, it can be seen that for compounds **8**–**10** the proportion of halogen···halogen contacts steadily increases with the atomic number, a trend that has already been observed and discussed in the packing diagrams (Figure 7B). In summary, compounds **8**–**10**, due to their isotypic crystal structure, exhibit strong similarities (Figure 8F) in their intermolecular contacts. Subtle differences arise that are related to the size and polarizability of the respective halogens. Compounds **6** and **7**, on the other hand, stand somewhat apart, as they favor significantly different intermolecular interactions due to the absence of a halogen substituent or the presence of a halogen with a small size and highly localized electron density, respectively.

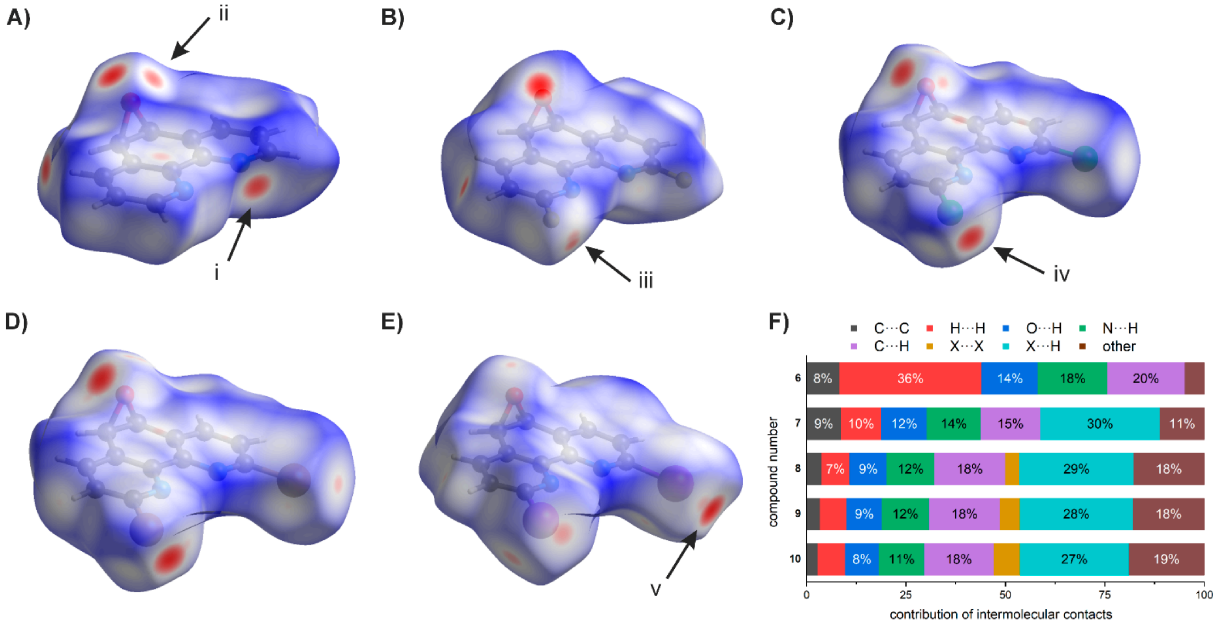

Figure 8. Hirshfeld surface plots (with highlighted short contacts) of compound **6** (A), compound **7** (B), compound **8** (C), compound **9** (D), compound **10** (E), and summary of the contribution of each intermolecular interaction for each compound (F). Highlighted are the points of strong interactions via the nitrogen atom (i) and the oxygen atom (ii) of compound **6**, via the fluorine atom of compound **7** (iii), via the chlorine atom of compound **8** (iv), and via the iodine atom of compound **10** (v).

In addition to fingerprint plots and the d_{norm} surface, analyzing the shape of the surface as a whole also allows for an interpretation of the interactions that occur. The shape index and the curvedness are particularly helpful in identifying stacking interactions because they pinpoint large planar areas with alternating concave and convex regions capable of forming such stacking interactions [44]. The alternating curvature on the flat surface of the molecules is most pronounced in compounds **6** and **7** (Figure S23A–D). Their tendency to interact via C···C bonds is also evidenced from the relatively high proportion (8–9%) of these interactions relative to the total intermolecular interactions (Figure 8F). In the case of the derivatives with heavier halogens **8**, **9** and **10,** it is noticeable that the Hirshfeld surfaces are less flat, and the alternately curved regions are less clearly defined, smeared across the molecule, and less localized on the rings (Figure S23E–J). This is also reflected in the significantly lower proportion of C···C interactions that these molecules form (2–3%) (Figure 8F). The halogen atoms appear to be responsible for this difference,

as they are increasingly deflected from the phenanthroline plane with increasing atomic number. The tendency of the epoxides to engage in stacking interactions is also evident in the 2D fingerprint plots of the reciprocal C···C interactions (Figures S18D–22D). The prominent signal at $d_e = d_i$ = 1.7–1.8 Å corresponds to an interplanar distance of 3.4 Å to 3.6 Å and is significant for stacking interactions [45].

To evaluate the close packing of the crystal structure, the close packing index (CP_i) can be used, which is derived from Hirshfeld surface analysis. Unlike Kitaigorodskii's packing index (KPI), this index often provides stronger correlations between different properties and also offers advantages when comparing multicomponent structures, such as co-crystallized solvents [28]. An overview of the data obtained can be found in the Supplementary Information (Table S1). To compare the effects of the solvent on the structure and its packing, the chloroform solvate structure [46] **6·CHCl$_3$** of epoxide **6** was compared with the hydrate structure **6·H$_2$O**. Within the series of halogenated epoxy derivatives **7**–**10**, it is evident that as the size of the halogen increases, the packing density of the structure based on the CP_i also increases. This could be due to halogen···halogen interactions, which are not found with fluorine-substituted epoxide **7** but whose contribution to the intermolecular interactions increases significantly with increasing atomic number of the halogen atom (Figure 8F). The Kitaigorodskii packing indices do not reflect this and instead show comparable packing without a clear trend. A similar pattern for these indices was also observed for hexahalobenzenes and is consistent with the trend seen in the structures of isostructural 2-haloaniline compounds [28].

With regard to the influence of solvent molecules, the crystal structure of **6·H$_2$O** is more densely packed than **6** due to the water molecules and the associated bridging hydrogen bonds, which is reflected in both the KPI and the CP_i (Table S1). Chloroform, on the other hand, presumably has the opposite effect due to weaker intermolecular interactions and results in a less densely packed crystal structure, which is also reflected here in both the KPI and the CP_i (Table S1).

3.6. Biological Activity

Since the biological effects of 1,10-phenanthroline have already been evaluated in various organisms, the influence of halogenation on these properties was of particular interest. Therefore, both phenanthroline derivatives and corresponding epoxides were investigated with respect to their effects on Vero cells, a non-cancerous kidney-derived cell line (Table 4). In these assays, 1,10-phenanthroline exhibited the lowest IC_{50} value with regard to cell viability. The halogenated phenanthroline derivatives showed increasing IC_{50} values with increasing electronegativity of the halogen substituent. For the corresponding epoxides, markedly higher IC_{50} values were observed compared with the non-epoxidized parent compounds. Therefore, only compounds **1** to **5** were screened additionally in selected cancer cell lines (Table 4). In general, activity was moderate compared to standard drugs and susceptibility varied among cell lines. Again, the effect on cell viability decreased with increasing electronegativity of the substituent. No difference was observed between cancerous cell lines and the non-cancerous Vero cells in their susceptibility to the treatment. Overall, these findings indicate that both halogenation and epoxidation reduce the cytotoxic activity of the phenanthroline scaffold.

Another distinctive feature occurred at higher concentrations of some of the derivatives. Compounds **1** and **6** (>100 µM), and to a lesser extent also compounds **7** and **8** (>250 µM), induced detachment of the cell monolayer. This phenomenon is typically related to a decrease in calcium-ion concentration in the cell culture medium [47,48]. EDTA, a chelating agent that was included for comparison, did not cause this effect and only led to a moderate reduction in viability in Vero cells (IC_{50} 254 µM).

Table 4. Cytotoxicity of halogenated 1,10-phenanthroline and 1,10-phenanthroline epoxide derivatives in cell lines Vero (African green monkey kidney cells), HepG2 (human liver carcinoma cells), A498 (human renal carcinoma cells), and A549 (human lung carcinoma cells). CI: confidence interval; n.d.: not determined due to inactivity of compound **7**.

Cell Line	Vero	HepG2	A498	A549
Compound	IC_{50} [μM] (95% CI)			
1	2.42 (1.91–2.95)	3.96 (2.87–5.43)	1.70 (0.96–2.97)	2.48 (2.03–3.25)
2	350 (288–429)	227 (195–260)	203 (74.2–749)	523 (436–715)
3	60.1 (51.3–70.9)	108 (73.0–155)	40.6 (22.9–70.8)	220 (118–471)
4	23.9 (16.5–34.9)	71.0 (52.2–94.3)	12.27 (6.03–28.0)	199 (145–278)
5	3.79 (3.45–4.13)	4.83 (3.94–5.61)	1.74 (0.95–3.23)	18.7 (9.12–42.4)
6	54.9 (47.4–62.7)	-	-	-
7	n.d.	-	-	-
8	246 (185–351)	-	-	-
9	392 (344–449)	-	-	-
10	285 (244–337)	-	-	-
Paclitaxel	0.604 (0.238–1.547)	0.071 (0.04–0.132)	-	-
Camptothecin	-	-	0.291 (0.171–0.495)	0.0029 (0.0018–0.0047)

In addition, the effects of the compounds on the growth of *Pseudomonas* and on biofilm formation were investigated. None of the phenanthroline derivatives exhibited any relevant inhibition of bacterial growth (all MICs > 256 μM) or biofilm formation (Figure S26).

4. Discussion

4.1. Role of Halogen Substituents on the Supramolecular Structure

The differences in the supramolecular structures are attributable to the various halogen substituents. In principle, the rigid phenanthroline system allows for both stacking interactions and C–H-based interactions. Halogen-based interactions emerge as the size and polarizability of the halogens increase. While the fluorinated compound exhibits no halogen···halogen interactions, significantly larger proportions can be quantified, particularly in the brominated and iodinated species (Figure 8F). These short-range interactions also extend throughout the supramolecular structure and ensure a well-defined architecture (Figure 7B). These interactions are of particular importance and are used in the engineering of structures [49].

4.2. Relationship Between Halogenation and Biological Activity

The results of the MTT assays for the parent compound, 1,10-phenanthroline (**1**), in HepG2, A498, and A549 cells were generally highly similar to those reported in previous studies [12,50]. Among the phenanthroline derivatives, variations in the cytotoxicity can be clearly correlated with the electronegativity of the respective substituents. This observation

can be rationalized on the basis of literature reports concerning the mode of action of related phenanthroline derivatives. In addition to mechanisms involving disruption of cellular integrity or DNA damage, phenanthrolines may act as chelators for metal cations in the cellular environment [51,52], including the sequestration of calcium ions from the medium. The ability of 1,10-phenanthrolines to complex alkali and alkaline-earth metal ions is well documented in the literature, both through crystallographic investigations of isolated complexes [53–55] and through the determination of complex formation constants [56–58]. In particular, stability studies indicate a pronounced preference of 1,10-phenanthroline derivatives for alkaline-earth metal ions [59,60]. Similarly, **1** has been reported to bind trace elements in cell culture media [61], which could serve as an explanation for our observation of cell detachment. However, this effect consistently occurred at concentrations exceeding the IC_{50} of **1** and was not observed in cells treated with the chelator EDTA. Thus, the impairment of cell viability at low micromolar concentrations may not be solely attributed to the depletion of metal ions from the culture medium, but may involve additional intracellular mechanisms. Moreover, the reduced availability of essential metal ions, such as iron or zinc, can disturb cellular homeostasis and consequently decrease cell viability, which has particularly been associated with antibacterial and antifungal effects of 1,10-phenanthroline [14,62,63]. The inactivity of compounds **1** to **10** against *P. aeruginosa* was therefore unexpected, although reports concerning antibacterial effects of **1** against this pathogen range from a moderate inhibition of growth and biofilm formation [64] to complete inactivity [65].

The donor properties of the chelating nitrogen atoms are strongly dependent on their electronic environment. The presence of adjacent, strongly electron-withdrawing substituents reduces the ability of the phenanthroline scaffold to coordinate metal ions, thereby interfering with the activity as chelators for metal cations. In line with reports relating the structures of phenanthroline derivatives to their antimicrobial activity [14], our study demonstrated that the effect on cell viability decreased with increasing electronegativity of the substituents in positions 2 and 9, supporting a depletion of essential metal cations by the phenanthroline derivatives as a plausible mechanism of action. This effect is significantly less pronounced with the phenanthroline epoxide derivatives, presumably due to their intrinsically lower cytotoxicity. The enhanced activities observed for 5,6-oxidized phenanthrolines may therefore be related to the chelating properties of the additional functional groups [13,14], rather than to the oxidation at position 5,6.

4.3. Outlook

Previous studies have already shown that the biological activity of phenanthroline-based molecules depends heavily on the cell line and microorganism being studied [4,8–13,65]. For this reason, the research will be expanded to include additional test systems. In the future, selected metal complexes will also be investigated, both in terms of biological activity and in terms of structure, since epoxidation introduces an additional stereochemical component.

Supplementary Materials: The following supporting information can be downloaded at: https://www.mdpi.com/article/10.3390/cryst16090582/s1. NMR data Figures S1–S17, Hirshfeld surface analysis Figures S18–S23, Table S1, and concentration-response curves Figures S24–S26.

Author Contributions: Conceptualization, V.S. and M.H.; Methodology, V.S. and M.H.; Formal analysis, M.L., V.S. and M.H.; Investigation, J.P., F.M., V.S. and M.H.; Data curation, J.P., F.M., M.L., V.S. and M.H.; Writing—original draft, M.H.; Writing—review & editing, J.P., F.M., M.L., V.S. and M.H.; Visualization, M.H.; Supervision, M.H.; Project administration, M.H. All authors have read and agreed to the published version of the manuscript.

Funding: This research was funded by University of Muenster and the funds of the chemical industry (VCI).

Data Availability Statement: The original contributions presented in this study are included in the article/Supplementary Material. Further inquiries can be directed to the corresponding author.

Acknowledgments: The authors thankfully acknowledge the support by Jens Müller and Andreas Hensel and thank for access to laboratories and chemicals. ChatGPT (GPT–5.5, OpenAI) was used to assist with orthographic mistakes and language improvement. The authors have reviewed and edited the output and take full responsibility for the content of this publication.

Conflicts of Interest: The authors declare no conflict of interest.

Abbreviations

The following abbreviations are used in this manuscript:

Cmpd	compound
DCM	dichloromethane
DMEM	Dulbecco's Modified Eagle's Medium
DMSO	dimethyl sulfoxide
eq.	equivalent(s)
EtOH	ethanol
EtOAc	ethyl acetate
HRMS	high-resolution mass spectrometry
IC_{50}	half-maximal inhibitory concentration
MIC	minimum inhibitory concentration
MTT	3-(4,5-dimethylthiazol-2-yl)-2,5-diphenyltetrazolium bromide
p.a.	*pro analysi*
PBS	phosphate-buffered saline
R_f	retention factor
rt	room temperature
sat.	saturated
TEA	triethylamine

References

1. Irving, H.; Mellor, D.H. 1002. The stability of metal complexes of 1,10-phenanthroline and its analogues. Part I. 1,10-Phenanthroline and 2,2′-bipyridyl. *J. Chem. Soc.* **1962**, 5222–5237. [CrossRef]
2. Brandt, W.W.; Dwyer, F.P.; Gyarfas, E.D. Chelate Complexes of 1,10-Phenanthroline and Related Compounds. *Chem. Rev.* **1954**, *54*, 959–1017. [CrossRef]
3. Lu, Y.; Conway-Kenny, R.; Twamley, B.; McGoldrick, N.; Zhao, J.; Draper, S.M. 1,10-Phenanthroline Ruthenium(II) Complexes as Model Systems in the Search for High-Performing Triplet Photosensitisers: Addressing Ligand versus Metal Effects. *ChemPhotoChem* **2017**, *1*, 544–552. [CrossRef]
4. Bonacorso, H.G.; Andrighetto, R.; Frizzo, C.P.; Zanatta, N.; Martins, M.A.P. Recent advances in the chemistry of 1,10-Phenanthrolines and their metal complex derivatives: Synthesis and promising applications in medicine, technology, and catalysis. *Targets Heterocycl. Syst.* **2016**, 1–27. [CrossRef]
5. Binacchi, F.; Cirri, D.; Bimbi, E.; Busto, N.; Pratesi, A.; Biver, T. Pd(II)/1,10-phenanthroline complexes bearing arene ligands: On the role of N- vs O-coordination to tune their cellular activity and binding ability towards DNA and RNA. *J. Inorg. Biochem.* **2025**, *262*, 112749. [CrossRef]
6. Páez, P.L.; Bazán, C.M.; Bongiovanni, M.E.; Toneatto, J.; Albesa, I.; Becerra, M.C.; Argüello, G.A. Oxidative Stress and Antimicrobial Activity of Chromium(III) and Ruthenium(II) Complexes on Staphylococcus aureus and Escherichia coli. *BioMed Res. Int.* **2013**, *2013*, 906912. [CrossRef]
7. Wesselinova, D.; Neykov, M.; Kaloyanov, N.; Toshkova, R.; Dimitrov, G. Antitumour activity of novel 1,10-phenanthroline and 5-amino-1,10-phenanthroline derivatives. *Eur. J. Med. Chem.* **2009**, *44*, 2720–2723. [CrossRef]
8. Bostancıoğlu, R.B.; Işık, K.; Genç, H.; Benkli, K.; Koparal, A.T. Studies on the cytotoxic, apoptotic and antitumoral effects of Au(III) and Pt(II) complexes of 1, 10-phenanthroline on V79 379A and A549 cell lines. *J. Enzym. Inhib. Med. Chem.* **2011**, *27*, 458–466. [CrossRef]

9. McCann, M.; Coyle, B.; McKay, S.; McCormack, P.; Kavanagh, K.; Devereux, M.; McKee, V.; Kinsella, P.; O'Connor, R.; Clynes, M. Synthesis and X-ray crystal structure of [Ag(phendio)2]ClO4 (phendio = 1,10-phenanthroline-5,6-dione) and its effects on fungal and mammalian cells. *BioMetals* **2004**, *17*, 635–645. [CrossRef]
10. Hara, T.; Matsuzaki, H.; Nakamura, T.; Yoshida, E.; Ohkubo, T.; Maruyama, H.; Yamamoto, C.; Saito, S.; Kaji, T. Cytotoxicity of zinc, copper and rhodium complexes with 1,10-phenanthroline or 2,9-dimethyl-1,10-phenanthroline in cultured vascular endothelial cells. *Fundam. Toxicol. Sci.* **2016**, *3*, 109–113. [CrossRef]
11. Ramos, M.C.; de Oliveira Neto, J.G.; Nogueira, C.E.S.; Reis, A.S.; de Sousa, F.F.; da Silva, L.M.; dos Santos, A.O. Structural, Vibrational, Thermal, and Cytotoxic Characterization of Aqua(1,10-Phenanthroline)(L-Serinato)Copper(II) Nitrate Complex Combined with DFT Calculations. *Cryst. Res. Technol.* **2023**, *58*, 2300240. [CrossRef]
12. Le, M.; Rathje, O.; Levina, A.; Lay, P.A. High cytotoxicity of vanadium(IV) complexes with 1,10-phenanthroline and related ligands is due to decomposition in cell culture medium. *J. Biol. Inorg. Chem.* **2017**, *22*, 663–672. [CrossRef]
13. Kellett, A.; Fichtner, I.; Kavanagh, K.; Devereux, M.; Pyrrho, A.S.; Romanos, M.T.V.; da Silva, B.A.; Santos, A.L.S.; McCann, M. In vitro and in vivo studies into the biological activities of 1,10-phenanthroline, 1,10-phenanthroline-5,6-dione and its copper(ii) and silver(i) complexes. *Toxicol. Res.* **2012**, *1*, 47–54. [CrossRef]
14. McCann, M.; Kellett, A.; Kavanagh, K.; Devereux, M.; Santos, A.L. Deciphering the antimicrobial activity of phenanthroline chelators. *Curr. Med. Chem.* **2012**, *19*, 2703–2714. [CrossRef]
15. Mai, F. Variablen zur Beeinflussung der Stabilität Metallvermittelter Basenpaare in DNA. Ph.D. Thesis, University of Münster, Münster, Germany, 2025.
16. Ammann, M.; Bäuerle, P. Synthesis and electronic properties of series of oligothiophene-[1,10]phenanthrolines. *Org. Biomol. Chem.* **2005**, *3*, 4143–4152. [CrossRef]
17. Krapcho, A.P.; Sparapani, S. Facile acidic hydrolysis and displacement reactions of 2-chloro-and 2,9-dichloro-1,10-phenanthroline. *J. Heterocycl. Chem.* **2009**, *45*, 1167–1170. [CrossRef]
18. Antkowiak, W.Z.; Antkowiak, R. On the Chlorine Addition to the C(5)-C(6) Bridge and the N-Oxidation of 1,10-Phenanthroline. *Heterocycles* **1998**, *2*, 893–909. [CrossRef]
19. Hubbard, A.J.; Jones, A.S.; Walker, R.T. An investigation by ^{1}H NMR spectroscopy into the factors determining the beta:alpha ratio of the product in 2′-deoxynucleoside synthesis. *Nucleic Acids Res.* **1984**, *12*, 6827–6837. [CrossRef]
20. *APEX6*, Version 2026.2-0; Bruker AXS Inc.: Madison, WI, USA, 2026.
21. *SAINT*, Version 8.42, Includes Xprep and SADABS, TWINABS; Bruker AXS Inc.: Madison, WI, USA, 2001.
22. Sheldrick, G.M. SHELXT—Integrated space-group and crystal-structure determination. *Acta Crystallogr. A Found. Adv.* **2015**, *71*, 3–8. [CrossRef]
23. Sheldrick, G.M. Crystal structure refinement with SHELXL. *Acta Crystallogr. C Struct. Chem.* **2015**, *71*, 3–8. [CrossRef]
24. Petříček, V.; Palatinus, L.; Plášil, J.; Dušek, M. JANA2020—A new version of the crystallographic computing system JANA. *J. Krist.* **2023**, *238*, 271–282. [CrossRef]
25. Kratzert, D. *FinalCif*. Available online: https://dkratzert.de/finalcif.html (accessed on 1 July 2026).
26. Diamond—Crystal and Molecular Structure Visualization, Crystal Impact—Dr. H. Putz & Dr. K. Brandenburg GbR, Kreuzherrenstr. 102, 53227 Bonn, Germany. Available online: https://www.crystalimpact.de/diamond (accessed on 1 July 2026).
27. Spackman, P.R.; Turner, M.J.; McKinnon, J.J.; Wolff, S.K.; Grimwood, D.J.; Jayatilaka, D.; Spackman, M.A. CrystalExplorer: A program for Hirshfeld surface analysis, visualization and quantitative analysis of molecular crystals. *J. Appl. Crystallogr.* **2021**, *54*, 1006–1011. [CrossRef]
28. Dahiya, R.; Sabu, S.; Mondal, S.; Thomas, S.P. Quantifying Packing Efficiency in Molecular Crystals: A Close Packing Index Based on Hirshfeld Surfaces. *Cryst. Growth Des.* **2025**, *25*, 8081–8088. [CrossRef]
29. Spek, A.L. Single-crystal structure validation with the programPLATON. *J. Appl. Crystallogr.* **2003**, *36*, 7–13. [CrossRef]
30. Mosmann, T. Rapid colorimetric assay for cellular growth and survival: Application to proliferation and cytotoxicity assays. *J. Immunol. Methods* **1983**, *65*, 55–63. [CrossRef]
31. Jeannot, K.; Plesiat, P. Drug susceptibility testing by dilution methods. *Methods Mol. Biol.* **2014**, *1149*, 49–58. [CrossRef]
32. Coffey, B.M.; Anderson, G.G. Biofilm formation in the 96-well microtiter plate. *Methods Mol. Biol.* **2014**, *1149*, 631–641. [CrossRef]
33. Desiraju, G.R.; Gavezzotti, A. Crystal structures of polynuclear aromatic hydrocarbons. Classification, rationalization and prediction from molecular structure. *Acta Crystallogr. Sect. B Struct. Sci.* **1989**, *45*, 473–482. [CrossRef]
34. Metrangolo, P.; Resnati, G. Type II halogen···halogen contacts are halogen bonds. *IUCrJ* **2013**, *1*, 5–7. [CrossRef]
35. Pedireddi, V.R.; Reddy, D.S.; Goud, B.S.; Craig, D.C.; Rae, A.D.; Desiraju, G.R. The nature of halogen · · · halogen interactions and the crystal structure of 1,3,5,7-tetraiodoadamantane. *J. Chem. Soc. Perkin Trans. 2* **1994**, *23*, 2353–2360. [CrossRef]
36. Xiao, Q.; Levine, M.S.; Iverson, B.L. Rethinking the Terms "π-Stacking" and "π–π Stacking" Again: A Proposal to Clarify the Language of Aromatic Interactions. *J. Am. Chem. Soc.* **2026**, *148*, 15331–15340. [CrossRef]
37. Decato, D.A.; Sun, J.; Boller, M.R.; Berryman, O.B. Pushing the limits of the hydrogen bond enhanced halogen bond—The case of the C–H hydrogen bond. *Chem. Sci.* **2022**, *13*, 11156–11162. [CrossRef]

38. van den Berg, J.-A.; Seddon, K.R. Critical Evaluation of C−H···X Hydrogen Bonding in the Crystalline State. *Cryst. Growth Des.* **2003**, *3*, 643–661. [CrossRef]
39. Zhang, Y.; Wang, W. Crystal structure of 2,9-dibromo-1,10-phenanthroline, C12H6Br2N2. *Z. Krist. New Cryst. Struct.* **2017**, *232*, 441–442. [CrossRef]
40. Nadeem, S.; Shah, M.R.; Ng, S.W. 2,9-Dichloro-1,10-phenanthroline. *Acta Crystallogr. E Struct. Rep. Online* **2009**, *65*, o922. [CrossRef]
41. Riwar, L.-J.; Trapp, N.; Kuhn, B.; Diederich, F. Substituent Effects in Parallel-Displaced π–π Stacking Interactions: Distance Matters. *Angew. Chem. Int. Ed.* **2017**, *56*, 11252–11257. [CrossRef]
42. Steiner, T. The Hydrogen Bond in the Solid State. *Angew. Chem. Int. Ed.* **2002**, *41*, 48–76. [CrossRef]
43. Spackman, M.A.; Jayatilaka, D. Hirshfeld surface analysis. *CrystEngComm* **2009**, *11*, 19–32. [CrossRef]
44. McKinnon, J.J.; Spackman, M.A.; Mitchell, A.S. Novel tools for visualizing and exploring intermolecular interactions in molecular crystals. *Acta Crystallogr. B* **2004**, *60*, 627–668. [CrossRef]
45. Mohamooda Sumaya, U.; Sankar, E.; Arasambattu MohanaKrishnan, K.; Biruntha, K.; Usha, G. Crystal structure determination, Hirshfeld surface analysis and energy frameworks of 6-phenylsulfonyl-6H-thieno [3,2-c]carbazole. *Acta Crystallogr. Sect. E Crystallogr. Commun.* **2018**, *74*, 878–883. [CrossRef]
46. Martí, A.A.; Mezei, G.; Maldonado, L.; Paralitici, G.; Raptis, R.G.; Colón, J.L. Structural and Photophysical Characterisation of fac-[Tricarbonyl(chloro)(5,6-epoxy-1,10-phenanthroline)rhenium(I)]. *Eur. J. Inorg. Chem.* **2004**, *2005*, 118–124. [CrossRef]
47. Kitajima, Y. New insights into desmosome regulation and pemphigus blistering as a desmosome-remodeling disease. *Kaohsiung J. Med. Sci.* **2012**, *29*, 1–13. [CrossRef]
48. Pokutta, S.; Weis, W.I. Structure and Mechanism of Cadherins and Catenins in Cell-Cell Contacts. *Annu. Rev. Cell Dev. Biol.* **2007**, *23*, 237–261. [CrossRef]
49. Aakeroy, C.B.; Baldrighi, M.; Desper, J.; Metrangolo, P.; Resnati, G. Supramolecular hierarchy among halogen-bond donors. *Chem. Eur. J.* **2013**, *19*, 16240–16247. [CrossRef]
50. Deegan, C.; McCann, M.; Devereux, M.; Coyle, B.; Egan, D.A. In vitro cancer chemotherapeutic activity of 1,10-phenanthroline (phen), $[Ag_2(phen)_3(mal)]\cdot 2H_2O$, $[Cu(phen)_2(mal)]\cdot 2H_2O$ and $[Mn(phen)_2(mal)]\cdot 2H_2O$ ($malH_2$=malonic acid) using human cancer cells. *Cancer Lett.* **2007**, *247*, 224–233. [CrossRef]
51. Burkitt, M.J.; Milne, L.; Nicotera, P.; Orrenius, S. 1,10-Phenanthroline stimulates internucleosomal DNA fragmentation in isolated rat-liver nuclei by promoting the redox activity of endogenous copper ions. *Biochem. J.* **1996**, *313*, 163–169. [CrossRef]
52. Roy, S.; Hagen, K.D.; Maheswari, P.U.; Lutz, M.; Spek, A.L.; Reedijk, J.; van Wezel, G.P. Phenanthroline derivatives with improved selectivity as DNA-targeting anticancer or antimicrobial drugs. *ChemMedChem* **2008**, *3*, 1427–1434. [CrossRef]
53. Neykov, M.; van Almsick, T.; Dimitrov, G. Synthesis, Spectral Properties and Crystal Structure of Calcium and Strontium Complexes of 1,10-Phenanthroline. *Z. Anorg. Allg. Chem.* **2006**, *632*, 1554–1559. [CrossRef]
54. Dimitrov, G.D.; Neykov, M.V. Alkaline earth metal ions mediated self-assembly in the presence of 1,10-phenanthroline, nitrate and tetrafluoroborate anions. *Spectrochim. Acta A Mol. Biomol. Spectrosc.* **2007**, *68*, 399–403. [CrossRef]
55. Murugavel, R.; Korah, R. Structural Diversity and Supramolecular Aggregation in Calcium, Strontium, and Barium Salicylates Incorporating 1,10-Phenanthroline and 4,4′-Bipyridine: Probing the Softer Side of Group 2 Metal Ions with Pyridinic Ligands. *Inorg. Chem.* **2007**, *46*, 11048–11062. [CrossRef]
56. Sugihara, H. 1,10-phenanthroline derivatives as ionophores for alkali metal ions. *Coord. Chem. Rev.* **1996**, *148*, 285–299. [CrossRef]
57. Bencini, A.; Lippolis, V. 1,10-Phenanthroline: A versatile building block for the construction of ligands for various purposes. *Coord. Chem. Rev.* **2010**, *254*, 2096–2180. [CrossRef]
58. Fromm, K.M. Chemistry of alkaline earth metals: It is not all ionic and definitely not boring! *Coord. Chem. Rev.* **2020**, *408*, 213193. [CrossRef]
59. Ghasemi, J.; Shamsipur, M. Spectrophotometric Study of Complex Formation between Some Alkali and Alkaline Earth Cations and Several Conventional (N,N), (N,O) and (O,O) Ligands in 95% Ethanol. *J. Coord. Chem.* **1993**, *28*, 231–236. [CrossRef]
60. González-González, J.; Nájera-Lara, M.; López-Ramírez, V.; Ramírez-Vázquez, J.A.; Segoviano-Garfias, J.J.N. Spectrophotometric determination of the formation constants of calcium(II) complexes with 2,2′-bipyridyl and 1,10-phenanthroline in acetonitrile. *Resour.-Effic. Technol.* **2016**, *2*, 240–246. [CrossRef]
61. Levina, A.; Crans, D.C.; Lay, P.A. Speciation of metal drugs, supplements and toxins in media and bodily fluids controls in vitro activities. *Coord. Chem. Rev.* **2017**, *352*, 473–498. [CrossRef]
62. Falconer, S.B.; Wang, W.; Gehrke, S.S.; Cuneo, J.D.; Britten, J.F.; Wright, G.D.; Brown, E.D. Metal-Induced Isomerization Yields an Intracellular Chelator that Disrupts Bacterial Iron Homeostasis. *Chem. Biol.* **2014**, *21*, 136–145. [CrossRef]
63. Brul, S.; Stratford, M.; van der Vaart, J.M.; Dielbandhoesing, S.K.; Steels, H.; Klis, F.M.; Verrips, C.T. The Antifungal Action of 1,10-o-phenanthroline and EDTA is Mediated Through Zinc Chelation and Involves Cell Wall Construction. *Food Technol. Biotechnol.* **1997**, *35*, 267–274.

64. Viganor, L.; Galdino, A.C.M.; Nunes, A.P.F.; Santos, K.R.N.; Branquinha, M.H.; Devereux, M.; Kellett, A.; McCann, M.; Santos, A.L.S. Anti-Pseudomonas aeruginosaactivity of 1,10-phenanthroline-based drugs against both planktonic- and biofilm-growing cells. *J. Antimicrob. Chemother.* **2016**, *71*, 128–134. [CrossRef]
65. Prisecaru, A.; McKee, V.; Howe, O.; Rochford, G.; McCann, M.; Colleran, J.; Pour, M.; Barron, N.; Gathergood, N.; Kellett, A. Regulating bioactivity of Cu2+ bis-1,10-phenanthroline artificial metallonucleases with sterically functionalized pendant carboxylates. *J. Med. Chem.* **2013**, *56*, 8599–8615. [CrossRef]